Highlights

A high-resolution photogrammetric workflow based on focus stacking for the 3D modeling of small Aegean inscriptions

Roberta Ravanelli,Lorenzo Lastilla,Silvia Ferrara

- This is the accepted manuscript of the article published by Elsevier in Journal of Cultural Heritage on 7 February 2022, doi: 10.1016/j.culher.2022.01.009, available online at: https://doi.org/10.1016/j.culher.2022.01.009.

A high-resolution photogrammetric workflow based on focus stacking for the 3D modeling of small Aegean inscriptions

Roberta Ravanelli[a], Lorenzo Lastilla[b] and Silvia Ferrara[a,*]

[a]Department of Classical Philology and Italian Studies (FICLIT), Alma Mater Studiorum – University of Bologna, 40126 Bologna, Italy
[b]Department of Computer, Control and Management Engineering Antonio Ruberti (DIAG) – Sapienza University of Rome, 00185 Rome, Italy

ARTICLE INFO

Keywords:
3D modeling
Cretan Hieroglyphic inscriptions
Linear A inscriptions
Macro-photogrammetry
Focus stacking

ABSTRACT

Any attempt of decipherment and language identification of the scripts from the Aegean dating to the second millennium BCE (namely Cretan Hieroglyphic and Linear A) has relied, until today, on traditional catalogues of inscriptions, consisting of incomplete or subjective 2D representations, such as photographs and hand-drawn copies, which are not suitable for documenting such three-dimensional writing systems. In contrast, 3D models of the inscribed media allow for an accurate and objective "autopsy" of the entire surface of the inscriptions. In this context, this work presents an efficient, accurate, high-resolution, and high-quality texture photogrammetric workflow based on focus-stacked macro images, designed for the 3D modeling of small Aegean inscriptions, to properly reconstruct their geometry and to enhance the identification of their signs, making their transcription as unbiased as possible. The pipeline we propose also benefits from a pre-processing stage to remove any coloration difference from the images, and a reliable and simple 3D scaling procedure. We tested this workflow on six inscribed artifacts (two in Cretan Hieroglyphic, three in Linear A, one uncertain), whose average size ranges approximately from 1 to 3 cm. Our results show that this workflow achieved an accuracy of a few hundredths of mm, comparable to the technical specifications of standard commercial 3D scanners. Moreover, the high 3D density we obtained (corresponding to the edge average length of the 3D model mesh), up to ≈ 30 μm, allowed us to reconstruct even the smallest details of the inscriptions, both in the mesh and in the texture layer of the 3D models.

1. Research aim

3D modeling techniques have never been applied systematically to the undeciphered Aegean inscriptions of the second millennium BC (Cretan Hieroglyphic, Linear A and Cypro-Minoan). Our results show that accurate and high-resolution 3D models with high-quality textures of small Aegean inscriptions can be efficiently produced using focus-stacked macro images within a ultra-close-range digital photogrammetric workflow, to achieve a thorough reconstruction of their geometry and reach unbiased identification of the shapes of the signs on the texts.

2. Introduction

The island of Crete in the second millennium BCE was a lively hub of script creation. Two writing systems, Cretan Hieroglyphic and Linear A were created and used for several centuries by palace elites to manage and monitor an ever-growing internal administration. To this day, both scripts remain undeciphered and as such their language (or indeed languages) have not yet been identified.

Cretan Hieroglyphic and Linear A can be considered as three-dimensional writing systems, because the media on which they are inscribed are three dimensional and their signs, being often deeply inscribed on clay, are three dimensional too [40]. Despite this, the traditional databases of Cretan Hieroglyphic and Linear A corpora, such as the *Corpus Hieroglyphicarum Inscriptionum Cretae* (CHIC, [50]) and the *Recueil des inscriptions en linéaire A* (GORILA, [26]), entirely rely on incomplete or subjective 2D representations of inscriptions, such as photographs and hand-drawn copies, both of which present several limitations.

Indeed, multiple photographs are arguably necessary to convey an accurate representation of an inscription distributed on different sides of a single object, and the whole process of image acquisition and processing is onerous and time-consuming.

Hand copies or drawings, in turn, convey the author's interpretation of the signs on the object [40]. Even if this is able to capture only the essential features of the inscriptions, hand-drawings are necessarily highly subjective (Figure 1), thus hindering scholars to establish an objective basis for sign identification.

In contrast, 3D models allow an accurate and objective documentation of the entire surface of the inscriptions [35, 55, 27, 22], from every point of view. One of the objectives of the ERC Consolidator project INSCRIBE — 'INvention of SCRIpts and their BEginnings' – is to produce the first corpus of 3D models of undeciphered scripts from the second millennium BCE Aegean (namely Cretan Hieroglyphic, Linear A and Cypro-Minoan) [36], which will involve hundreds of inscribed objects and will surpass the limitations of traditional databases.

Today, 3D modeling can rely on established geomatic techniques, such as photogrammetry and 3D scanning. The high-resolution workflow proposed here is based on ultra-

*Corresponding author at: Department of Classical Philology and Italian Studies (FICLIT), Alma Mater Studiorum – University of Bologna, 40126 Bologna, Italy.
E-mail address: s.ferrara@unibo.it (S. Ferrara).
ORCID(s): 0000-0001-5540-6241 (R. Ravanelli); 0000-0003-1099-6270 (L. Lastilla); 0000-0003-2498-7666 (S. Ferrara)

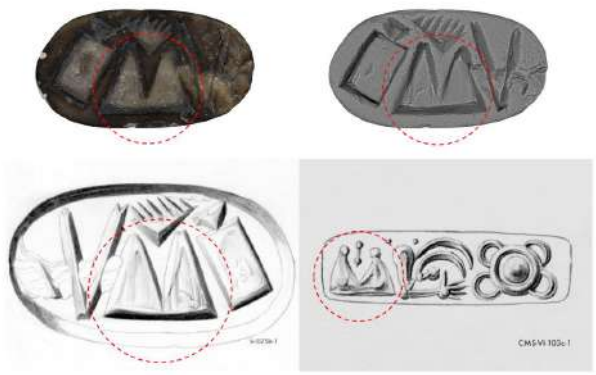

Figure 1: Example of stylistic variability in the transcription of sign CH 034 between seals CMS-V-025b-1 (lower left image) and CMS-VI-103c-1 (lower right); for seal CMS-V-025b-1, the 3D model rendered with the photogrammetric texture (upper left) and the Radiance Scaling shader (upper right) [63] is shown (the transcriptions [21] are mirrored with respect to the object, to represent the impression of the seals).

close-range digital photogrammetry [45] and, for the sake of this contribution, it was tested on six inscribed artifacts (two in Cretan Hieroglyphic, three in Linear A, one uncertain), to assess the accuracy and the resolution of the 3D models and to evaluate the reconstruction of the signs. Further details on the objects, whose average size ranges approximately from 1 to 3 cm, are given in Section 4.1.

In particular, the combination of focus stacking [24] and ultra-close-range digital photogrammetry based on macro lenses[23] allowed to produce the best results in terms of texture restitution [59] while matching the accuracy (ranging from a tenth of mm to few hundredths of mm) and resolution of commercial 3D scanners [35, 41], and with a less expensive equipment.

Finally, the 3D modeling workflow described here is enriched by two additional practical measures with respect to other photogrammetric pipelines:

- a pre-processing stage to minimize any coloration difference from the images;
- a well-founded 3D scaling – and accuracy assessment – from a geomatic point of view, by using a high number of scale bars – uniformly distributed over at least two non-parallel planes – to scale each 3D model and to assess its accuracy.

3. Related work

3.1. Digitization of archaeological artifacts

Traditional documentation methods of the inscriptions, such as photographs and hand-drawings, have now been surpassed by advanced digital techniques, such as Reflectance Transformation Imaging (RTI), ultra-close-range digital photogrammetry and 3D scanning, which are fast becoming the standard methods in humanities and cultural heritage [15, 22]. Among these, RTI [49] is a Computational Photography technique widely used for documenting surfaces with incisions, such as rock art, wall graffiti and epigraphs [62]. However, RTI is a 2.5D technique: it increases the perception of depth through lighting control, highlighting details and morphological changes of the recorded surfaces [62, 22]. In addition, a synthetic version of RTI can be performed by changing the lighting orientation on high resolution 3D models, since 3D models also encode the directions of the normals of the object surface – that is, the information captured by RTI –, as shown by Figure 2, where the same 3D model of the stone seal CMS V Suppl. IB, no. 310 is rendered through the Electronic Microscope shader available on MeshLab [16], and is illuminated from different directions. Most importantly, RTI cannot be considered as a spatial measurement technique.

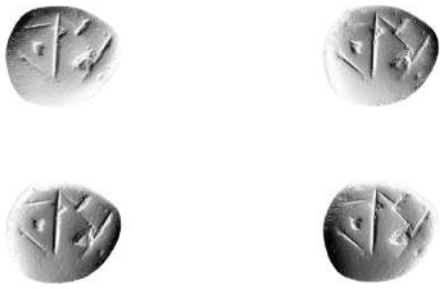

Figure 2: Synthetic version of RTI for the stone seal CMS V Suppl. IB, no. 310.

Therefore, 3D modeling maintains the advantages offered by RTI in terms of documentation and inspection of the inscriptions, while adding several benefits, such as the possibility of analyzing the true 3D morphology of the signs and carrying out accurate spatial measurements.

In the wider context of the 3D documentation of archaeological artifacts, the most widespread solutions are 3D scanning and ultra-close-range digital photogrammetry [57, 43]. 3D scanning systems, such as laser scanners and the majority of non-laser-based scanners, are active sensors. Currently, most of the 3D scanners adopted in cultural heritage for reconstructing small objects with high precision rely on the active triangulation principle, and many among them employ the structured-light technology [12, 22, 35, 55]. In [22] and [12], the same hand-held structured-light scanner was used to generate 3D models of a limestone epigraph and two cuneiform inscriptions to study their text. In [19], a Roman wall decorated with mosaics was reconstructed with a laser scanner and its 3D model contributed to evaluate the state of degradation of the mosaic. In [35], a small stone object, carved along its exterior skin, was modeled in 3D with a structured-light scanner; the model served to gauge the function of the object. In [27], a blue LED scanner was used to produce the 3D models of few Linear B tablets, to test for the presence or absence of strokes. In [55], a high-resolution 3D

model of a Maya *stela* was collected using a structured light scanner and employed to enhance the legibility of the text via rendering filters. All these results are testament to the effectiveness of 3D scanners which, however, are expensive devices, especially if we consider the low cost of standard photogrammetry equipment.

Moreover, 3D scanners are delicate instruments which employ prefixed scan volumes and operative distances, thus are hardly adaptable to scan objects of different sizes and materials from those for which they are designed. For example, it is well known that structured-light scanners have problems to model shiny and dark objects, such as some of the stone seals analyzed in this study. Finally, most of the metrology 3D scanners are unable to capture colour information [10] and, when available, their *texture* restitution is not comparable to that of photogrammetry [59], whose high quality *texture* allows for an in-depth documentation of the artifacts and becomes a key factor whenever the signs are lightly sketched on their surface. For all these reasons, photogrammetry is the optimal solution for the purposes of closely analyzing, correctly reading, and transcribing the small Aegean inscriptions considered here.

3.2. Photogrammetry

Unlike 3D scanning, photogrammetry is a passive technique that relies on the ambient light reflected by the specimen to collect range data through the passive triangulation principle [45, 44]. Nowadays, most of the photogrammetric software applications leverage the "Structure from Motion (SfM) – Multi-View stereo" joint approach [65, 9]. Starting from a set of images captured moving the camera around the subject and framing the scene from different but partially overlapping views, SfM photogrammetry allows to estimate their internal and external orientation parameters, together with the low-density point cloud of the object, simultaneously and automatically, through a sparse bundle adjustment system [60, 65]. This system employs robust algorithms for keypoint matching and selection, for error minimization through non-linear least-squares solution in the estimate of camera pose orientation, for triangulation to compute the 3D point positions and incrementally reconstruct scene geometry [65, 12, 9, 47]. Several studies are available on the 3D reconstruction of small archaeological objects with ultra-close-range digital photogrammetry. In [15], photogrammetry is used to analyze two Roman epigraphs with 3D models, but no accuracy assessment is performed. In [52], a portable photogrammetry rig for a fast and systematic capture of images is tested on small lithic cores. In [18], a fast and low-cost photogrammetric system for precise acquisition of small artifacts is presented together with an automated processing workflow based on open source algorithms. The work of [45], instead, systematically reviews and analyzes applications, technical implementations, and performances of ultra-close range photogrammetry in skeletal anthropology. In [59], a controlled methodology for artifacts with dimensions of 5–10 cm, able to match the accuracy typically obtained with commercial scanning systems, is proposed. In all these cases, however, the texture quality and/or the 3D geometry resolution of the resulting 3D models are still not sufficient to model the complexity of the small details of our inscriptions. These problems can be effectively addressed by using macro lenses, which are characterized by high resolving power (systems equipped with macro lenses could achieve micrometric optical resolution up to 2 μm [51, 23]) but a shallow Depth of Field (DoF).

3.2.1. *Focus Stacking photogrammetry*

Focus stacking constitutes an effective solution to overcome the problem of the limited DoF of the macro lenses and to extend their sharpness area, avoiding any loss of quality due to diffraction [24]. Like RTI, also Focus Stacking belongs to the family of Computational Photography techniques: it leverages a sequence of images - a stack - (representing the same view of a given object) captured with different (increasing or decreasing) focus distances in order to obtain a single image with an extended DoF [41]. Focus stacking was successfully applied to the photogrammetric 3D modeling of archaeological artifacts, with an accuracy ranging from few tenths to few hundredths of mm [24, 17, 41, 39]. In particular, one of the first applications of the focus stacking technique to the photogrammetric 3D reconstruction of small sized objects is presented in [24], where Gallo et al. achieved an accuracy of about 10 microns on a volume with a diagonal of 25 mm. However, the authors evaluated the accuracy on the planar surfaces of certified gauge blocks, which are characterized by a 3D geometry simpler than our inscriptions. Clini et al. [17] used the focus stacking technique to reconstruct a 3D model of a small statue (8.7×2.6 cm) with a mean error and a standard deviation of about 10 and 50 microns, respectively. Nevertheless, this result was achieved after applying a scaling factor derived from a reference 3D model generated with a laser scanner. Kontogianni et al. [39] tested the focus stacking technique using a full-frame camera equipped with a normal lens (50 mm). They obtained a 3D model characterized by an absolute mean error of few microns and a standard deviation of about 70 microns, but the resolution and the quality of the texture are not sufficient to model the complex details of our inscriptions.

The combination of photogrammetry and focus stacking, however, presents some issues which must be carefully taken into account before and during image acquisition. In general, focus stacking can have an effect on the estimate of the camera calibration parameters of the output images: in practice, some assumptions on the principal point coordinates and focal length can be considered [24] . Secondly, the camera settings should be properly designed, by choosing, for example, a suitable aperture value to avoid diffraction and longer exposure times, with higher risks of blur due to vibrations [24]. For the same purpose of reducing any vibration or camera-object relative micro-movement as much as possible, which could undermine the quality of the resulting images, focus stacking requires a stable setup, and, possibly, to remotely control the camera by a PC. Anyway, micro-move-

ments are effectively managed by focus stacking algorithms, which align the images within a single stack by performing scale transformations, translations and rotations [24]. Finally, another problem which can arise when adopting focus stacking is the presence of artifacts in the output images: this problem, however, can be solved by properly setting the parameters of the focus stacking method and by ensuring DoF overlap between consecutive images within a single stack.

4. Materials and methods

4.1. Inscriptions

The material we used as sample for our workflow consists of six objects engraved or inscribed in the undeciphered Aegean scripts of the second millennium BCE, Cretan Hieroglyphic and Linear A, from the island of Crete. The Cretan Hieroglyphic inscriptions are housed in museums on Crete, in Agios Nikolaos and Rethymno, and the Linear A ones in Rome, at the National Museum of Prehistory and Ethnography "Luigi Pigorini" (Museo delle Civiltà). The first two plus the uncertain item consist of semi-precious stone seals that were used by scribes or administrators to be impressed on clay documents in the economic runnings of the so-called 'Minoan' palaces, and the other three are clay nodules pierced on their length, so that a cord or strings could run through them, similarly to store documents together.

These are the objects:

Cretan Hieroglyphic:

- CMS-V-025b (Archaeological Museum of Agios Nikolaos) [21];
- VRY S (4/4) 01 (Archaeological Museum of Rethymno) [29];

Linear A:

- 71950 (HT Wa 1014, Pigorini Museum) [26];
- 71965 (HT Wa 1561, Pigorini Museum) [26];
- 71975 (HT Wa 1779, Pigorini Museum) [26];

Uncertain:

- CMS V Suppl. IB, no. 310 (Archaeological Museum of Rethymno) [21].

4.2. Photogrammetric setup and survey

The 3D documentation methodology for the complex artifacts analyzed in this study must satisfy some fundamental requirements. First, the lighting should be as uniform as possible, avoiding sharp shadows [17, 59, 41]. Considering the small average size of the artifacts (1-3 cm) and of the inscribed signs (0.5-2 mm), even small lighting variations can affect the alignment process, the accuracy of the 3D model and the quality of the texture restitution.

Second, motion blur and camera vibrations must be avoided, since focus stacking assumes that images belonging to the same stack - a set of images captured from the same view but with different focus distances - share the same camera view [24]; a static background with respect to the object is necessary to prevent errors in image alignment. In general, a regular acquisition scheme is recommended [17], since it prevents motion blur and increases the procedure time efficiency.

Then, a well-designed system to scale the 3D model (and to check the accuracy of the scaling procedure) is of the utmost importance: it can be obtained by placing several scale bars around the object, and, most of all, by ensuring that they are well distributed on the 3D space embracing the object itself (Figure 4b). Indeed, a high number of scale bars, uniformly distributed over at least two non parallel planes, must be used to scale each 3D model and to assess its accuracy. This is a standard procedure for the materialization of geodetic 3D reference frames. Despite this, many photogrammetric workflows often suggest using scale bars placed just on one plane or on parallel planes, therefore guaranteeing a 2D scaling only.

To match these requirements, we opted for a Canon EOS 2000D camera, equipped with a macro lens (Canon EF 100mm f/2.8L Macro IS USM) and mounted on a tripod (Figure 3). The choice of an APS-C (Advanced Photo System - Classic) format based camera fit perfectly to our purpose: indeed, APS-C cameras ensure a wider DoF than full frame ones (at the same aperture and for the same Field of View), thus they are more suitable for macro-photography. The artifacts were placed inside a white diffuser photobox with small LED lights, to ensure overhead illumination and a neutral ambient light. To shed frontal light on the object from the front and sides, we placed two LED spotlights (mounted on tripods) near the camera, so that the light direction formed, respectively, $\pm 45°$ with the camera axis (Figure 3). All the light sources were employed with a color temperature of about 6000K. Moreover, we used a X-Rite ColorChecker Nano (24×40 mm) target, namely a planar rectangular 4 by 6 array of patches of neutral colors, well-spaced and ranging from white to black [46] (Figure 5). By pre-processing raw images, the ColorChecker was useful to remove, as much as possible, any coloration difference in the images, and to retrieve the most faithful image colors.

To give the 3D models an accurate scale in the three dimensions, we placed the objects either on small bricks covered with graph paper and fixed on a turntable or directly on the graph paper covering the turntable. In both cases, by acquiring the object by multiple sides, we were able to materialize a proper 3D scale (Figure 4). We opted for this solution instead of Coded Targets (CTs) because of the difficulty of employing the latter when dealing with small archaeological objects as the ones involved in our study [24], and of creating calibration sets (like the system described in [59]) of CTs with the required accuracy, despite the fact that CTs can be automatically detected and matched on source photos by Metashape [5].

The turntable kept the camera location and view direction fixed, while rotating the object: in this way, we were

Table 1
Settings and main details of the acquisition stage, for each object.

Object	ISO [-]	Shutter speed [s]	Aperture value [-]	No. of rotations [-]	No. of image stacks [-]	Avg. No. of images per stack [-]	Avg. length (per rotation) [h:min]
CMS-V-025	100	1/100	f/5.6	3	78	11	0:43
71950	100	1/60	f/5.6	3	75	13	0:52
71965	100	1/60	f/5.6	3	72	15	0:56
71975	100	1/60	f/5.6	3	68	13	0:52
VRY S (4/4) 01	100	1/100	f/5.6	2	48	20	1:07
CMS V Suppl. IB, no. 310	100	1/100	f/5.6	3	61	11	0:41

able to reduce the camera vibrations and to increase stability.

Figure 3: Photogrammetric setup.

Based on this setup, it was possible to capture each side of the object with a complete rotation of the turntable, corresponding to approximately 22/26 image stacks per object side. The number of rotations depends on the object shape.

The image stacks necessary to the focus stacking processing stage were acquired in raw format through a remote control system and the Helicon Remote software [31]. For each stack, and thus for each position of the turntable, the focus preview tool of Helicon Remote was used to select the nearest and the farthest focusing points of the scene. Then, we manually set the value of the interval parameter, namely the movement of the lens between two adjacent shots, and the software automatically calculated the required number of shots on the basis of the two focusing endpoints previously selected, the current aperture and the focal length of the lens [32]. In particular, we used the DoF calculator of HeliconRemote to estimate the DoF in focusing steps (lens ring motor steps which regulate the entity of the lens rotation during focus) on the basis of the current aperture, the focal length and the lens model (through the correction factor), in order to set an interval between shots lower than this value. In this way, the limited but different sharp areas in the multiple images of the stack can overlap and, when combined, produce a perfectly sharp image of the object of interest [32].

In Table 1, the settings and main details of the acquisition stage are detailed for each object.

The average number of images per stack and the average acquisition length (per rotation[1]) are obviously correlated: the higher the average number of images composing a stack, the longer the duration of a single rotation around the object (given $\approx$ 24 stacks per rotation).

Moreover, the average number of images per stack depends on the object size, on the working distance of the camera [39] and on the DoF of the optical system (which can be optimized by adjusting the shutter speed and the aperture value [24]). As to the experiments presented here, the working distance of the camera affects the average number of images per stack more than any other factor, since the optical parameters and the average size of the object are constant through all the case studies.

In terms of optical system parameters, the sensor sensitivity was set to the native value for our device (which corresponds, in this case, to ISO 100) to ensure the lowest digital noise level and to provide clear detailed images [39]; the shutter speed and the aperture value were optimized with respect to the lighting condition. In particular, the aperture was set to f/5.6, our lens sweet spot (that is, the sharpest aperture of the lens) [33]. Sharp images are indeed necessary not only for focus stacking, but also for obtaining high quality texture in the final 3D models.

Finally, the time needed to capture a single object (two hours and twenty minutes per object, on average) exceeds other methods proposed in the literature which do not rely on focus stacking. This time, however, is necessary to guarantee the level of resolution, accuracy and precision we expected for the geometry and the texture of the 3D models, as we will see in the following Sections.

4.3. Image processing

4.3.1. Focus stacking processing

The multiple images of each view captured at different focus distances were processed together as image stacks to produce new - focused - images with a greater DoF to be used as input to the photogrammetric software (after the application of the radiometric calibration, see Section 4.3.2). In particular, we used the commercial software Helicon Focus [30] to process the raw image stacks: we selected the 7.0.2

[1]More precisely, the average acquisition length (per rotation) is a weighted arithmetic mean: each rotation duration is weighted according to the number of image stacks for that rotation.

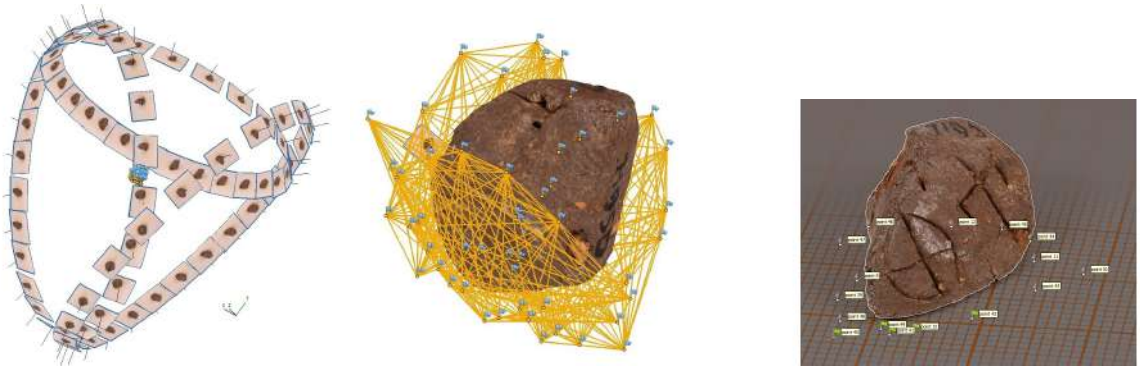

(a) (b) (c)

Figure 4: Clay nodule 71950: (a) view of the 3D model and of the camera positions estimated during the image alignment by Metashape; (b) zoom on the 3D model and the scale bars, placed on three different planes; (c) one of the focused images used to produce the 3D model: 16 markers were collimated on the considered plane (one of the three) materialized by the graph paper; the mask automatically obtained with the *Import from Model* option on Metashape is shown as a dark overlay.

version since it is the only one able to preserve the EXIF data – needed by Metashape for estimating the focal length of the lens (see Section 4.3.3) – of the original images in the focused images.

The focus stacking processing in Helicon Focus is based on three parameters [34, 41]:

1. *rendering method*, i.e. the focus stacking algorithm;
2. *radius*, i.e. the number of pixels around each pixel that are used to calculate its contrast;
3. *smoothing*, i.e. how the sharp areas are combined.

We opted in all cases for the *rendering method* based on the depth map computation, to preserve the original colors and contrast, and because, considering our case study, the images would not have sudden and frequent high DoF variations. Small values of *radius* (which was set to 3 pixels) and *smoothing* (which was set to 4) were always chosen, after having checked the absence of halo in the computed images. The focus stacking process took about one minute for each image stack, depending on the number of images contained in the stack (the assessment was carried out on a Dell XPS 8930 machine). The focused images were finally exported as raw image files.

4.3.2. Radiometric processing

The focused images were radiometrically calibrated to retrieve the most faithful colors for the 3D models. Furthermore, minimizing the differences in terms of texture in the same areas of the object simplifies the matching stage within Metashape. Common approaches for precise color reproduction based on digital images employ ICC color profiles or camera profiles [48]. Therefore, for each object we built a custom color profile, specific to the camera and the lighting conditions, with the ColorChecker Camera Calibration version 2.0 [66] software, using the focused image of the ColorChecker as input (Figure 5).

Finally, the custom color profile was applied to the corresponding set of images with Adobe Photoshop Lightroom [1], which was also used to develop the raw images, exporting them without compression in JPEG format, usable by Metashape. Overall, the radiometric calibration took approximately five minutes per 3D model.

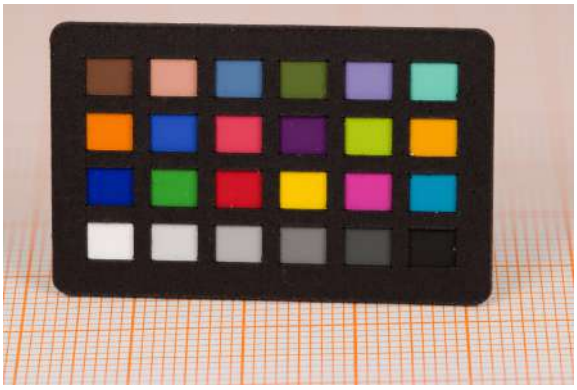

Figure 5: Focused image of the X-Rite ColorChecker Nano target, captured for calibrating the colors.

4.3.3. Photogrammetric processing

The photogrammetric processing was carried out with the commercial software Agisoft Metashape version 1.6.5 [3], formerly known as Agisoft Photoscan, based on the SfM technique. The software was run locally on a Mac Pro (Late 2013) and a Dell XPS 8930, both equipped with 64 GB of RAM. The focused images, radiometrically calibrated, were given as input to Metashape as standard images, and no constrains were considered for the estimation of the camera parameters.

To prevent the background (specific for each rotation around the object, due to the presence of the graph paper (Figure 4)) from negatively affecting the alignment stage, we automatically generated accurate masks for the images through the *Import from Model* option of Metashape (Figure 4c). In particular, we separately masked each subset of images – corresponding to a specific rotation around the object

Table 2
Total duration of the photogrammetric processing carried out on Metashape (excluding the masking stage).

Object	Total time [h:min:s]
CMS-V-025b	0:59:09
VRY S (4/4) 01	0:31:41
CMS V Suppl. IB, no. 310	0:19:18
71950	0:50:11
71965	0:47:37
71975	0:41:29

– based on the low-quality mesh generated from that subset (this operation took about seven minutes per subset). The masks allowed to limit the search for feature points only to the shape of the considered object (Figure 4c) and thus to process all the images in a single chunk. This allowed to obtain a better accuracy and quality of the 3D model, if compared to the alternative chunking method (separate processing of the subsets) which often requires markers to be added manually [8].

For each object, the alignment was carried out with the *Highest* accuracy, meaning that the images are up-sampled by a factor of 4 [5]. The main requirement to adopt this option, that is to use very sharp images [5], was satisfied by choosing optimal values of aperture (set to the lens sweet spot), DoF interval, and a focus stacking rendering method able to preserve the original image contrast. The alignment was refined by optimizing the camera parameters on the most reliable points of the sparse cloud [7], according to the Brown's distortion model implemented in Metashape [14, 5]. In particular, we removed through the *Gradual Selection* filter uncertain tie-points characterized by values of *reconstruction uncertainty* (ratio of the largest semi-axis to the smallest semi-axis of the error ellipse of the triangulated 3D point coordinates), *reprojection error* (maximum reprojection error in normalized units across all images where the tie-point was measured), and *projection accuracy* (average image scale at which the image coordinates of the tie-point were measured) higher than a threshold [3], set to 9 for *reconstruction uncertainty* and *projection accuracy* and to 0.5 for *reprojection error*.

As to the dense cloud generation, we selected *Ultra-High* quality and *Aggressive* filtering mode for all the case studies, to maximize the resolution while sorting out the outliers [6]. We also computed the point confidence for each point of the dense point clouds, which represents the number of depth maps used for the given point generation [7], to automatically clean the dense clouds from the less reliable points.

For the same purpose of maximizing the 3D model resolution, we produced the meshes (using the dense clouds as sources [6]) with *High* quality and Interpolation *Enabled*.

Finally, for each object we generated the model texture according to the default set of parameters. In Table 2, we recall the duration of the whole photogrammetric processing (excluding the masking stage).

To give the 3D models an accurate and precise scale in a 3D reference frame, we used the graph paper to collimate several markers uniformly around the objects on the aligned images (Figure 4c). Each marker was collimated on (at least) five different images.

In particular, we chose a different number of markers for each model (Table 3), depending on the number of rotations around the object in the acquisition stage and on the position of the graph paper (either on the bricks or directly on the turntable).

Based on the Euclidean distance between each pair of markers belonging to the same plane (Figure 4b), we were able to assign many scale bars to the 3D models. More specifically, given n points collimated on the same plane, we were able to assign m scale bars to the model:

$$m = \frac{n \cdot (n-1)}{2} \tag{1}$$

The scale bars were partitioned in two independent subsets, according to the Hold-Out Validation (HOV) method [13], which is easy to implement, but needs a high number of scale bars. In particular, half of the scale bars were used as control bars to assign the scale to each 3D model and half as check bars to assess the accuracy of the 3D model itself. For all the 3D models, the partition was carried out in such a way that both the control bars and the check bars were well distributed around the object of interest, on the area covered by the graph paper of each plane (see Section 4.2 and Figure 4b). The number of scale bars for each 3D model is recalled in Table 3.

The need for a high number of scale bars to satisfy the HOV method requirements must be verified, however, in terms of impact on the scale accuracy. To quantitatively assess the effect of our choice on the accuracy assessment, we performed a specific test discussed in Section 5.2.1.

5. Results and discussion

The 3D models we obtained are shown in Tables 4 (seals CMS-V-025b, VRY S (4/4) 01, CMS V Suppl. IB, no. 310) and 5 (nodules 71950, 71965, 71975). They were rendered within the MeshLab software framework through the standard texture shader and (to increase sign legibility) through the Radiance Scaling [63] shader – which allows depicting shape through shading via the modification of light intensities around specific features like concavities and convexities [42]. These shaders help to evaluate the reconstruction of the signs, comparing them to the transcription available in the traditional corpora (Tables 4 and 5). The visual comparison shows how the 3D models faithfully reconstruct the inscriptions, thanks to the high resolution of the texture and of the 3D geometry, allowing to disambiguate proper signs from random scratches on the object surface and to evaluate possible corrections to tweaking of current drawings. The 3D models are available for an interactive inspection on the INSCRIBE 3D Interactive Web Viewer [37], a WebGL

Table 3
Number of markers, number of scale bars and marker distribution in the 3D space.

Object	Number of markers [-]	Number of planes [-]	Markers per plane [-]	Number of scale bars [-]
CMS-V-025b	47	3	15 - 15 - 17	346
VRY S (4/4) 01	48	3	20 - 18 - 10	388
CMS V Suppl. IB, no. 310	34	2	17 - 17	272
71950	50	3	16 - 17 - 17	392
71965	50	3	16 - 17 - 17	392
71975	50	3	16 - 17 - 17	392

3D viewer based on 3DHOP (3D Heritage Online Presenter) [53, 54] for basic 3D visualization and on the Cuneiform-WebGLViewer [20] for Radiance Scaling.

5.1. 3D density assessment

The geometric density of our 3D models was quantitatively assessed: in Table 6, we summarize the number of points of the dense cloud and of faces and vertices; moreover, the surface of the models and the number of faces and vertices per mm^2 are reported. The differences in terms of point, face and vertex density can be attributed to:

- the number of images per object (Table 1): the higher this value, the higher the number of reliable tie-points – this could explain why the 3D model of VRY S (4/4) 01 is the least dense;
- the material of the objects: the clay nodules present a very rich, detailed and opaque texture, whereas the stone seals are shiny and are characterized by a more uniform texture, which hinders the matching process. This does not apply, however, to the CMS V Suppl. IB, no. 310: this small seal has a more compact, spherical shape, which allows to frame the same point from multiple views during a single rotation around the object, and thus simplifies the search for tie-points during the alignment and dense cloud generation stages.

In Table 7, further details on the meshes are reported. In particular, the bounding box size and diagonal were computed after the mesh alignment to Principal Axes (through a filtering algorithm available on MeshLab). The volumes, instead, were computed with the MeshLab *Compute Geometric Measures* filter, having previously closed the holes of some of the meshes (marked with an asterisk in Table 7). The impact of this correction on the volume estimate is, in any case, negligible, given the precision of the estimate itself.

The face and vertex densities reported in Table 6 highlight the high resolution of the 3D models we obtained, as demonstrated by Tables 4 and 5. The point density of a 3D model is indeed strictly connected to its geometric resolution: the high density of our 3D models allows to capture details up to ≈ 30 μm and, therefore, to densely reconstruct even the smallest elements of the inscriptions, such as, for example, the scribe's fingertip impression, clearly distinguishable in the meshes of the 3D models of the clay nodules (Table 5 and by using the Radiance Scaling option on the INSCRIBE 3D Interactive Web Viewer [37]).

Finally, even though the blending procedure of the photographic texture tends to smooth out the high frequencies, the finer details of the objects are still visible in the texture layer of their 3D models (Figure 1, Tables 4 and 5), thanks to the focus stacking technique and, therefore, to the high optical resolution of the input images.

5.2. Accuracy assessment

Once the 3D models were scaled by means of the control bars (see Section 4.3.3), the accuracy of the photogrammetric workflow was assessed via two independent approaches. First, the accuracy of each 3D model was evaluated by computing the Root Mean Square Error (RMSE) of the check bars (Section 5.2.1). Then, only for the three nodules[2], we carried out a second assessment by comparing each photogrammetric 3D model with a reference 3D model captured with a commercial structured-light scanner (Section 5.2.2).

5.2.1. Check bars

As stated in Section 4.3 and summarized in Table 3, the scale bars were placed on three non-parallel planes for all the objects, with the exception of the seal CMS V Suppl. IB, no. 310, for which only two planes were used. The average RMSE computed over all the check bars of each object is shown in Table 8, together with the respective relative errors (computed as the percentage ratios between the RMSE and the average mesh bounding box size – derived from Table 7) and the average reprojection error of the tie-points and markers over all the images.

It is known that the reprojection error of a point is related to the accuracy of the image alignment: an high reprojection error usually indicates poor localization accuracy of the corresponding point projections during the matching process [5]. Indeed, the reprojection error is the distance between the point on the image where a reconstructed 3D point is projected and the original projection of that 3D point detected on the image and used as a basis for the 3D point reconstruction procedure [5]. The accuracy of the alignment

[2]The stone seals were not reconstructed with the structured-light scanner since they are particularly shiny and therefore difficult to be correctly modelled.

Table 4
3D models of the seals CMS-V-025b, VRY S (4/4) 01 and CMS V Suppl. IB, no. 310 and comparison with the documentation available in [21, 29]. The 3D models are available for an interactive visualization and analysis on the INSCRIBE 3D Interactive Web Viewer [37].

Seal	Documentation [21, 29]			3D model	
	Photo	Drawing	Impression	Texture layer	Radiance Scaling
CMS-V-025b					
VRY S (4/4) 01					
CMS V Suppl. IB, no. 310					

Table 5
3D models of the nodules 71950, 71965 and 71975 and comparison with the documentation available in GORILA [26]. The 3D models are available for an interactive visualization and analysis on the INSCRIBE 3D Interactive Web Viewer [37].

Nodule	Face with sign				Face with seal impression	
	GORILA [26]		3D model		3D model	
	Photo	Drawing	Texture layer	Radiance Scaling	Texture layer	Radiance Scaling
71950		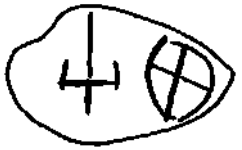		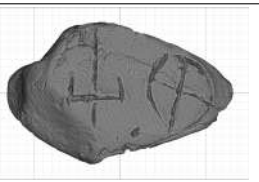		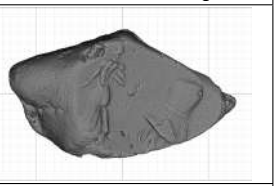
71965		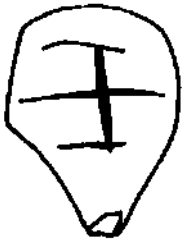				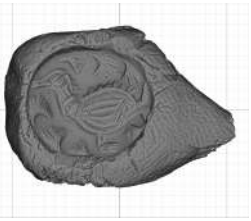
71975				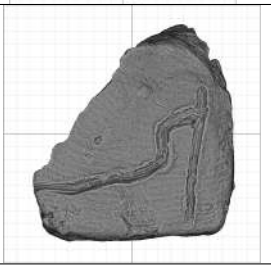	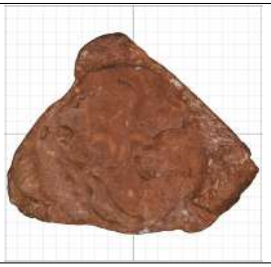	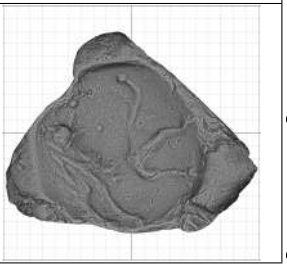

Table 6
Details of the geometry of the 3D models.

Object	Points [-]	Faces [-]	Vertices [-]	Mesh surface area [cm^2]	Face density [1/mm^2]	Vertex density [1/mm^2]	Edge average length [cm]
CMS-V-025b	9,759,428	1,951,885	976,214	9.01	2166	1083	0.0035
VRY S (4/4) 01	6,591,786	1,318,356	659,344	6.25	2109	1055	0.0036
CMS V Suppl. IB, no. 310	10,331,266	2,063,812	1,032,264	4.05	5096	2549	0.0023
71950	16,170,869	3,234,172	1,617,338	10.27	3149	1575	0.0029
71965	19,198,836	3,839,767	1,920,095	8.81	4358	2179	0.0025
71975	15,856,941	3,171,387	1,585,830	7.57	4189	2095	0.0026

Table 7
Further details on the mesh geometry of the 3D models.

	Mesh volume [cm^3]	Mesh bounding box size [cm × cm × cm]	Mesh bounding box diagonal [cm]
CMS-V-025b*	1	$1.1 \times 1.0 \times 2.2$	2.7
VRY S (4/4) 01*	1	$0.9 \times 0.9 \times 1.9$	2.3
CMS V Suppl. IB, no. 310	1	$0.9 \times 1.1 \times 1.1$	1.8
71950	2	$1.6 \times 1.5 \times 2.7$	3.4
71965*	1	$1.0 \times 1.6 \times 2.2$	2.9
71975*	1	$1.2 \times 1.6 \times 2.0$	2.8

has therefore an impact on the 3D geometry reconstruction, whose accuracy was however evaluated independently by means of the RMSE on the check bars, namely the RMSE of the residuals between the known lengths of the check bars and the corresponding Euclidean distances measured on the 3D model. It is important to recall that the check bars were not used for the scaling process (see Section 4.3.3). In particular, the results show how the photogrammetric workflow we adopted ensured the alignment of all the images, with an average reprojection error of the tie-points that is remarkably lower than half a pixel for all the 3D models considered. Moreover, the markers that were manually identified and used to set the scale bars (Figure 4c) are characterized by an average error that is lower than half a pixel for all the 3D models, with the exception of the seal CMS-V-025b, for which the error is still lower than one pixel.

As regards the accuracy of the 3D geometry reconstruction, on average the RMSE of the check bars is around $2 \cdot 10^{-2}$ mm over all the 3D models. In terms of relative errors, the results are very similar for the 3D models of nodules 71965 and 71975, whereas the 3D model of nodule 71950 fared slightly worse, comparable to the one of seal CMS-V-025b. The 3D model of seal CMS V Suppl. IB, no. 310 is, conversely, the most accurate, possibly thanks to its compact, spherical shape, which allows to frame the same area from several views, whereas the 3D model of VRY S (44) 01 shows the highest relative error.

Finally, as previously anticipated, to quantitatively assess the effect of the choice of such a high number of scale bars on the accuracy assessment, we carried out the following test (for the clay nodule 71965 only)[3]: we split the available scale bars (392, for this object) in two equally numerous sets (one for the control, and one for the check bars); then, we randomly sampled k control and k check bars per plane, with $k = 1, ..., \frac{n \cdot (n-1)}{4}$, where n is the number of markers per plane (Figure 4b) and we computed the RMSE for all the check bars based on the coordinate reference system produced through all the control bars. For each value of k, we repeated the test 100 times. This way, we were able to investigate the relationship between the number of scale bars and the RMSE from a statistically relevant point of view. The result of the test is visible in Figure 6: the plot shows the mean RMSE of the check bars over the 100 iterations for each number of scale bars involved in the scaling/accuracy assessment stage, together with the respective uncertainty (one standard deviation of uncertainty is represented). Figure 6 clearly highlights how the RMSE keeps stable with a slightly decreasing trend as the number of scale bars increases, and a higher number of bars helps to reduce the uncertainty on the accuracy assessment.

5.2.2. Mesh to cloud comparison

We used the V-GER ScanRider 1.2 structured-light scanner [61] to collect the reference 3D models of the three nodules, due to its high performances - of the order of few tens of microns (Table 9) - in terms of nominal precision, accuracy and resolution, necessary to reconstruct the smallest details of the inscribed objects under investigation [2, 42, 41, 43]. After an initial stage of calibration, the scanning process was performed using the most accurate scan-

[3]The code is available at https://github.com/INSCRIBERC/Metashape-Utils.

Table 8
Average RMSE and relative error for check bars, and tie-point and marker average reprojection errors.

	Aligned cameras [-]	Tie-points average reprojection error [pixels]	Markers average reprojection error [pixels]	RMSE check bars [mm]	Relative error check bars [%]
CMS-V-025b	78/78	0.261	0.833	0.02	0.15
VRY S (4/4) 01	48/48	0.302	0.390	0.03	0.25
CMS V Suppl. IB, no. 310	61/61	0.318	0.384	0.01	0.09
71950	75/75	0.268	0.425	0.02	0.13
71965	72/72	0.246	0.368	0.01	0.09
71975	68/68	0.252	0.486	0.02	0.09
Mean		0.275	0.481	0.02	0.13
Std.Dev.		0.026	0.162	0.01	0.06

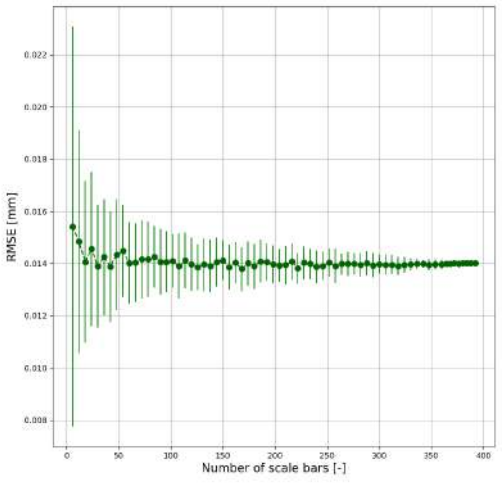

Figure 6: Relationship between the RMSE of the check bars and the number of scale bars involved in the scaling/accuracy assessment process (one standard deviation of uncertainty is represented).

ning volume (Table 9). Then, within the SpaceRider software, the raw scans were co-registered with an average alignment error of $1 \cdot 10^{-2}$ mm, and subsequently cleaned, fused and smoothed, producing the reference 3D models for the three nodules.

To evaluate the geometric accuracy of the 3D models produced with the developed workflow, we computed the signed distances (positive outside and negative inside the reference mesh surface) of each vertex of the specific photogrammetric model from the nearest mesh of the respective reference 3D model, following the procedure described in [56]. Before computing the distances, the parameters of a roto-translation without scale adjustment were estimated through the Iterative Closest Point (ICP) algorithm [11] for co-registering the 3D models in the same reference system. In this way, the distance of the points of the photogrammetric 3D models from the reference meshes can be considered as representative of the errors with respect to the commercial structured-light scanner used to collect the reference 3D models.

Table 9
Scanning volume specifications (volume 1) of the V-GER ScanRider 1.2 scanner [61] used to collect the reference 3D models of the three nodules.

ScanRider 1.2 specifications	
Volume maximum size [mm]	$66 \times 50 \times 50$
Object maximum size [mm]	66
Standard resolution [mm]	≤ 0.05
Precision [mm]	up to 0.03
Mean error [mm]	up to 0.01
Working distance [mm]	120

Therefore, for each 3D model, the distance distribution was characterized through the statistical parameters [38] shown in Table 10. In addition to the standard statistical parameters able to describe normal error distributions, such as the mean, the standard deviation (Std.Dev.) and the RMSE, we also computed the robust statistical parameters for non-normal error distributions, *i.e.* the median (50^{th} percentile), the Normalized Median Absolute Deviation (NMAD) and the Linear Errors with 68% and 90% of probability (LE68 and LE90). Indeed, the median is a robust measure of central tendency, being affected by outliers less than the mean, and the NMAD can be regarded as an estimate for the standard deviation for heavy tail distributions [64]: in case of normally distributed errors, the standard deviation is identical to NMAD whereas, in case of larger discrepancies, the standard deviation will be larger than NMAD.

The results are summarized in Table 10 and in Figures 7, 8, 9 which show the error maps of each photogrammetric 3D model in different areas of the object and the overall distance distribution. The colour scale represents the distance of each point from the reference mesh, expressed in mm, set within an interval centered on the mean and ranging from -3 Std.Dev. to 3 Std.Dev.

Table 10
Error statistics computed over the distances between the vertices of the photogrammetric mesh and the reference structured-light mesh for each nodule.

	Mean [mm]	Std.Dev. [mm]	RMSE [mm]	Median [mm]	NMAD [mm]	LE68 [mm]	LE90 [mm]	Max [mm]	Min [mm]
71950	0.02	0.02	0.03	0.02	0.01	0.02	0.03	0.13	-0.10
71965	0.01	0.02	0.03	0.01	0.01	0.01	0.03	0.15	-0.15
71975	0.01	0.01	0.02	0.01	0.01	0.01	0.02	0.07	-0.05
Mean	0.01	0.02	0.02	0.01	0.01	0.01	0.03	0.12	-0.10

Table 10 shows that the 3D models are reconstructed with an average accuracy (RMSE) of about $2 \cdot 10^{-2}$ mm, a value perfectly in agreement with the results of the validation on the check bars. At the same time, the results denote the presence of outliers: the Std.Dev. is indeed higher than the NMAD. In the 3D model of the nodule 71965, the outliers are principally located in the low tail of the error distribution (Figure 8d), but their effect on the median is negligible (it is comparable to the mean, indeed), at least to the order of magnitude of $1 \cdot 10^{-2}$ mm. These points correspond mostly to an area of the nodule that is not reconstructed by the structured-light scanner and to a lesser extent to areas of the sign (Figure 8a) where the width of the incision is less wide and where, therefore, the shadows may have had a negative impact on the matching process.

In the 3D models of nodules 71950 and 71975 (Figures 7d, 9d), the outliers are instead approximately located in both the high and the low tail of the error distribution: also in this case, however, the mean is comparable to the median both for the model of clay nodule 71975 and 71950.

With the exception of the few points of the 3D model 71965 placed in proximity of the incision, for all the three nodules, the largest errors are located in the areas where there is not a direct correspondence between the photogrammetric 3D model and the reference one. For example, this is the case of the areas near and inside the holes of the nodules (Figures 7c, 8c and 9c), due to occlusion issues. Other outliers are placed in correspondence of the dark inventory number label (Figures 8c and 9c), which is difficult to be correctly reconstructed with the structured-light scanner. Lastly, to examine the 3D models more closely, we extracted the sections reported in Figures 10, 11 and 12: for all the nodules, the sections show an optimal agreement between the reference and the photogrammetric mesh, highlighting once again the accuracy of the proposed photogrammetric workflow.

Finally, it is worth noticing how the simple 3D scaling procedure, based on the use of a high number of scale bars, well distributed on the 3D space embracing the object of interest by means of common sheets of graph paper, achieved an accuracy of a few hundredths of millimeter, in agreement with the values reported in [39, 24].

6. Conclusions and future porspects

In this work, an ultra-close-range digital photogrammetric workflow based on the use of focus-stacked macro images was planned and tested on six inscribed artifacts, whose average size ranges from 1 to 3 cm. The workflow was specifically designed for the 3D reconstruction of small inscriptions inscribed or engraved in the undeciphered scripts from the Aegean dating to the second millennium BCE with high accuracy and high resolution.

Main results. First, we performed a pre-processing stage to remove, as much as possible, any coloration difference from the images. Then, we carried out a simple 3D scaling procedure employing common sheets of graph paper. In particular, the graph paper was placed over different non-parallel planes to uniformly cover the 3D space embracing the artifacts to be modeled with a high number of scale bars.

The 3D density and the geometric accuracy of the 3D models were quantitatively assessed and the reconstruction of their signs was evaluated and compared to the available drawings. The results show how the proposed photogrammetric workflow achieved an accuracy of a few hundredths of millimeter, comparable, in terms of order of magnitude, to the accuracy of the commercial structured-light scanner used as reference, and a 3D density (up to ≈ 30 μm) able to unveil even the smallest details of the inscriptions, both in the mesh and in the texture layer of the 3D models. This was possible thanks to the high quality of the images captured with the focus stacking technique, which allowed to preserve the tiny details of the objects under investigation in the focused images.

Limitations and possible improvement of the methodology. This approach has however the disadvantage of the time needed for both the acquisition process of the image stacks and their whole processing. If, on the one hand, it is not convenient to reduce the image acquisition times because this would happen at the expense of a loss of detail, due to the the diffraction effects connected to the increase of the DoF [24], on the other hand, the photogrammetric processing can be shortened employing cloud-based photogrammetric software environments, such as the one, for example, operated by Agisoft [4]. Indeed, cloud-based photogrammetric software environments host the processing logic and data storage capabilities into remote servers equipped with high performing

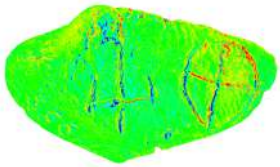

(a)

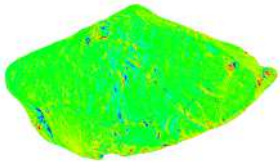

(b)

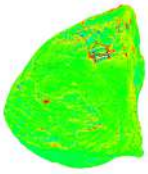

(c)

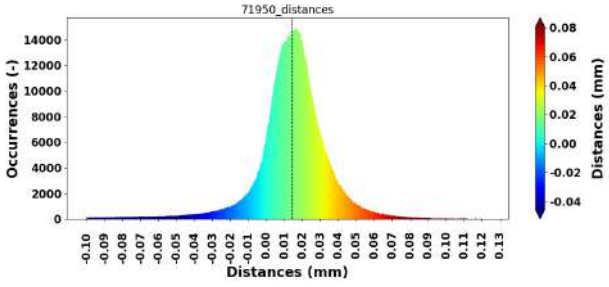

(d)

Figure 7: 71950 error map: distances (in mm) between the vertices of the photogrammetric mesh and the reference structured-light mesh; (a) face with sign incision; (b) face with seal impression; (c) outliers; (d) error distribution.

(a)

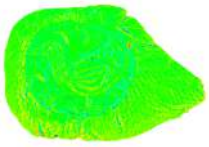

(b)

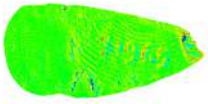

(c)

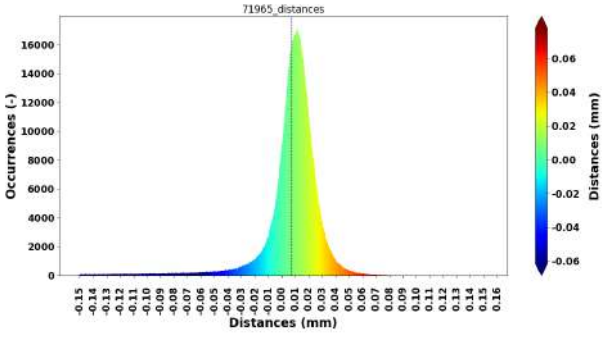

(d)

Figure 8: 71965 error map: distances (in mm) between the vertices of the photogrammetric mesh and the reference structured-light mesh; (a) face with sign incision; (b) face with seal impression; (c) outliers; (d) error distribution.

hardware. However, issues related to the upload of the images online must be taken into consideration, since a good internet connection, which is not always available in a museum, is needed to transfer the data from local machines to the cloud. Furthermore, most of the photogrammetric cloud providers require an additional fee with respect to the standard licence in order to have processing priority, unlimited cloud storage and/or unlimited hours of processing.

-The next step of our research will also focus on the improvement of the validation method used for the partition of the scale bars between control bars and check bars (see Section 4.3.3). The HOV method was indeed selected in this first stage of our research because it has the advantage of being easy to implement, but it also presents some drawbacks, such as the need for a high number of scale bars and the dependence of the accuracy evaluation on the scale bars selected as check bars [13]. For this reason, in future we plan to apply the Leave-One-Out (LOO) method, a special case of the k-fold cross-validation method, for the partition of the scale

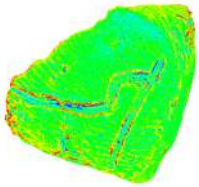

(a)

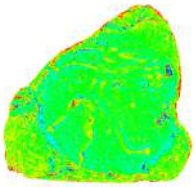

(b)

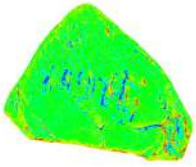

(c)

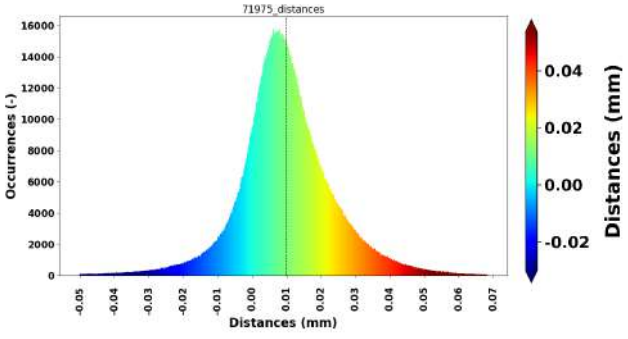

(d)

Figure 9: 71975 error map: distances (in mm) between the vertices of the photogrammetric mesh and the reference structured-light mesh; (a) face with sign incision; (b) face with seal impression; (c) outliers; (d) error distribution.

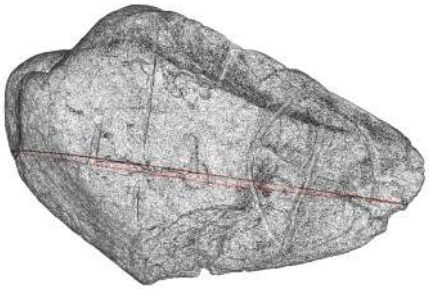

(a)

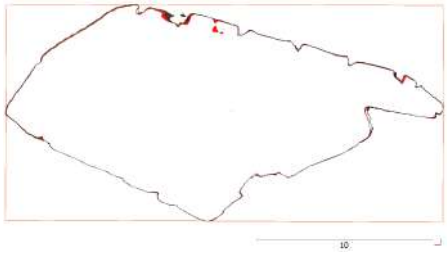

(b)

Figure 10: 71950 section: (a) overall view of the section, (b) reference mesh in red, photogrammetric mesh in brown (the scale is expressed in mm).

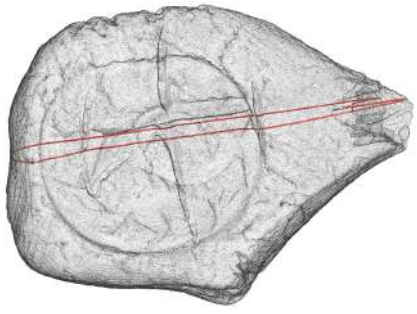

(a)

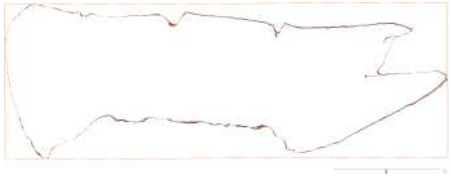

(b)

Figure 11: 71965 section: (a) overall view of the section, (b) reference mesh in red, photogrammetric mesh in brown (the scale is expressed in mm).

bars between control bars and check bars [13].

Future prospects. In conclusion, our workflow produced a 3D digital twin of each inscription, characterized by a high degree of detail and, therefore, compatible with the requirements of high standard paleographic analyses. In this way, specialists can perform remote and unbiased "autopsy" of the entire surface of the inscriptions, directly based on the 3D model, from any point of view, instead of relying on incomplete or subjective 2D representations of the inscriptions.

A crucial step towards the understanding of the undeciphered Aegean scripts is to provide tools for the scientific community to converge on shared analyses. Thanks to the increasing amount of 3D libraries and projects suitable for scientific metrological analyses (such as [53] and [20]), including shading capabilities, measurement and lighting tools, we were able to develop the INSCRIBE 3D Interactive Web Viewer [37], where the 3D models produced in this work

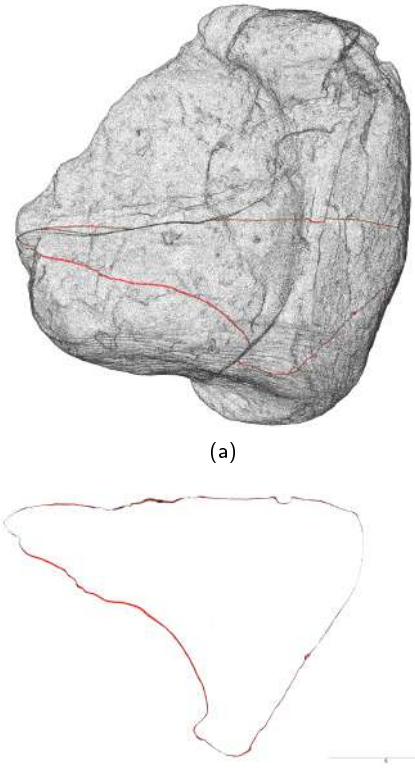

(a) (b)

Figure 12: 71975 section: (a) overall view of the section, (b) reference mesh in red, photogrammetric mesh in brown (the scale is expressed in mm).

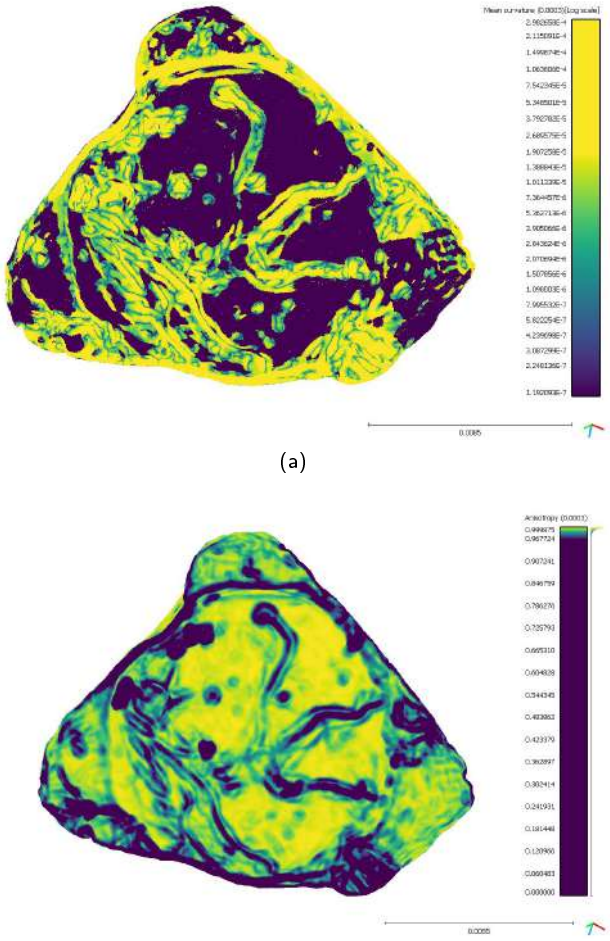

(a) (b)

Figure 13: Representation of two geometric features – mean curvature and anisotropy – of the 71975 clay nodule 3D model.

are publicly available. This platform extends the results of our work beyond the mere documentation, allowing a minute "reading" of the signs inscribed and incised on the objects, potentially correcting previous interpretations, in order to reach unparalled digital transcriptions.

Moreover, digital enhancing algorithms, such as Radiance Scaling and Electronic Microscope, the lighting control capabilities of the available 3D model processing software tools, or further processing of the 3D models, *e.g.* the generation of orthophotos or Digital Surface Models, can be employed to solve common legibility problems, ensuring an accurate and reliable analysis of the inscribed documents and serving as basis for upgraded transcriptions.

Finally, the benefits of 3D modeling of ancient scripts for paleographic analyses are not limited to the accurate representation and the enhanced readability of the inscriptions only, but also include the automatic transcription of the inscriptions themselves. As suggested in [28], indeed, machine learning methods can be used to classify and detect structural features of the point clouds based on geometric features, such as the mean curvature and the anisotropy – represented in Figures 13a and 13b for the 71975 clay nodule 3D model, and computed through the eigenvalues and eigenvectors of the local structure tensor on CloudCompare [25]. In this way, it would be ideally possible to detect and extract the signs from the 3D model, and to project them separately in a 2D space (for a clear example of the role of the curvature parameter in the projection of 3D inscriptions in a 2D space, see [58]).

Funding

This research is part of the ERC Project “INSCRIBE. Invention of Scripts and Their Beginnings” (awarded to Silvia Ferrara). The project has received funding from the European Research Council (ERC) under the European Union’s Horizon 2020 Research and Innovation Program (Grant Agreement No. 771127).

This research was partially supported by Sapienza University of Rome, through the PhD fellowship and "Avvio alla ricerca 2019" funding granted to Lorenzo Lastilla.

Declarations of interest

The authors declare no conflict of interest.

Acknowledgements

We are thankful to Dr. Anastasia Tzigounaki, Director of the Archaeological Museum of Rethymno and Dr. Chryssa Sofianou, Director of the Archaeological Museum of Agios Nicholaos, Crete. We are also very grateful to the National Museum of Prehistory and Ethnography "Luigi Pigorini" (Museo delle Civiltà), Rome, for their kind assistance during repeated visits, in particular to Dr. Mario Mineo.

References

[1] Adobe, 2020. Adobe Photoshop Lightroom. https://www.adobe.com/products/photoshop-lightroom-classic.html. URL: https://www.adobe.com/products/photoshop-lightroom-classic.html. accessed: 2020-09-24.

[2] Affatato, S., Valigi, M., Logozzo, S., 2017. Wear distribution detection of knee joint prostheses by means of 3D optical scanners. Materials 10, 364. doi:10.3390/ma10040364.

[3] Agisoft, a. Agisoft Metashape. URL: https://www.agisoft.com/. accessed: 2020-09-24.

[4] Agisoft, b. Agisoft Cloud. https://agisoft.freshdesk.com/support/solutions/folders/31000118608. URL: https://agisoft.freshdesk.com/support/solutions/folders/31000118608. online; accessed October, 2021.

[5] Agisoft, c. Agisoft metashape user manual: Professional edition, version 1.6. 2021.

[6] Agisoft, 2020a. 3d model reconstruction. https://agisoft.freshdesk.com/support/solutions/articles/31000152092-3d-model-reconstruction. Online; accessed March, 2021.

[7] Agisoft, 2020b. Aerial data processing (with GCPs) - Orthomosaic & DEM generation. https://agisoft.freshdesk.com/support/solutions/articles/31000153696-aerial-data-processing-with-gcps-orthomosaic-dem-generation. Online; accessed January, 2021.

[8] Agisoft, 2020c. How to build a complete (360 degree) model of an object. URL: https://agisoft.freshdesk.com/support/solutions/articles/31000155265-how-to-build-a-complete-360-degree-model-of-an-object. online; accessed February, 2021.

[9] Aicardi, I., Chiabrando, F., Maria Lingua, A., Noardo, F., 2018. Recent trends in cultural heritage 3D survey: The photogrammetric computer vision approach. Journal of Cultural Heritage 32, 257–266. doi:https://doi.org/10.1016/j.culher.2017.11.006.

[10] Albertin, F., Ruberto, C., Cucci, C., Callieri, M., Potenziani, M., Siotto, E., Pingi, P., Scopigno, R., Bettuzzi, M., Brancaccio, R., et al., 2021. "Ecce Homo" by Antonello da Messina, from non-invasive investigations to data fusion and dissemination. Scientific Reports 11, 1–18. doi:s41598-021-95212-2.

[11] Besl, P.J., McKay, N.D., 1992. A method for registration of 3-d shapes. IEEE transactions on pattern analysis and machine intelligence 14, 239–256. doi:10.1109/34.121791.

[12] Bitelli, G., Borghi, B., Francolini, C., Galletti, F., 2020. New hypotheses and interpretations regarding the Longobard Basin in the "Jerusalem" of Bologna supported by 3D surveying methodologies. Journal of Cultural Heritage 46, 226–234. doi:https://doi.org/10.1016/j.culher.2020.04.005.

[13] Brovelli, M.A., Crespi, M., Fratarcangeli, F., Giannone, F., Realini, E., 2008. Accuracy assessment of high resolution satellite imagery orientation by leave-one-out method. ISPRS Journal of Photogrammetry and Remote Sensing 63, 427–440. URL: https://www.sciencedirect.com/science/article/pii/S0924271608000191, doi:https://doi.org/10.1016/j.isprsjprs.2008.01.006.

[14] Brown, D.C., 1971. Close-range camera calibration, photogrammetric engineering. Engineering and Remote Sensing 37, 855–866.

[15] Carrero-Pazos, M., Espinosa-Espinosa, D., 2018. Tailoring 3D modelling techniques for epigraphic texts restitution. Case studies in deteriorated roman inscriptions. Digital Applications in Archaeology and Cultural Heritage 10, e00079. doi:10.1016/j.daach.2018.e00079.

[16] Cignoni, P., Callieri, M., Corsini, M., Dellepiane, M., Ganovelli, F., Ranzuglia, G., 2008. MeshLab: an Open-Source Mesh Processing Tool, in: Scarano, V., Chiara, R.D., Erra, U. (Eds.), Eurographics Italian Chapter Conference, The Eurographics Association. doi:10.2312/LocalChapterEvents/ItalChap/ItalianChapConf2008/129-136.

[17] Clini, P., Frapiccini, N., Mengoni, M., Nespeca, R., Ruggeri, L., 2016. SfM technique and focus stacking for digital documentation of archaeological artifacts. The International Archives of the Photogrammetry, Remote Sensing and Spatial Information Sciences 41. doi:10.5194/isprs-archives-XLI-B5-229-2016.

[18] Collins, T., Woolley, S.I., Gehlken, E., Ch'ng, E., 2019. Automated Low-Cost Photogrammetric Acquisition of 3D Models from Small Form-Factor Artefacts. Electronics 8, 1441. doi:10.3390/electronics8121441.

[19] D'Aranno, P.J.V., De Donno, G., Marsella, M., Orlando, L., Renzi, B., Salviani, S., Santarelli, M.L., Scifoni, S., Sonnessa, A., Verri, F., Volpe, R., 2016. High-resolution geomatic and geophysical techniques integrated with chemical analyses for the characterization of a roman wall. Journal of Cultural Heritage 17, 141–150. doi:10.1016/j.culher.2015.06.005.

[20] Fisseler, D., Müller, G.G.W., Weichert, F., 2017. Web-Based Scientific Exploration and Analysis of 3D Scanned Cuneiform Datasets for Collaborative Research. Informatics 4. URL: https://www.mdpi.com/2227-9709/4/4/44, doi:10.3390/informatics4040044.

[21] Förtsch, R., . idai.objects arachne (arachne) database. https://arachne.uni-koeln.de/drupal/. URL: https://arachne.uni-koeln.de/drupal/. data retrieved: 2020-08-07.

[22] Francolini, C., Marchesi, G., Bitelli, G., 2018. High-resolution 3d survey and visualization of mesopotamian artefacts bearing cuneiform inscriptions, in: 2018 Metrology for Archaeology and Cultural Heritage (MetroArchaeo), IEEE. pp. 183–187. doi:10.1109/MetroArchaeo43810.2018.13617.

[23] Galantucci, L.M., Guerra, M.G., Lavecchia, F., 2018. Photogrammetry applied to small and micro scaled objects: A review, in: Ni, J., Majstorovic, V.D., Djurdjanovic, D. (Eds.), Proceedings of 3rd International Conference on the Industry 4.0 Model for Advanced Manufacturing, Springer International Publishing, Cham. pp. 57–77. doi:10.1007/978-3-319-89563-5_4.

[24] Gallo, A., Muzzupappa, M., Bruno, F., 2014. 3D reconstruction of small sized objects from a sequence of multi-focused images. Journal of Cultural Heritage 15, 173–182. doi:10.1016/j.culher.2013.04.009.

[25] Girardeau-Montaut, D., 2019. Cloud compare—3D point cloud and mesh processing software. Version 2.10.2. URL: https://www.danielgm.net/cc/. accessed October 2021.

[26] Godart, L., Olivier, J.P., 1976. Recueil des inscriptions en linéaire A: Études crétoises. Geuthner (Paris).

[27] Greco, A., Flouda, G., 2018. The linear B PA-I-TO epigraphic project. Annuario della Scuola Archeologica di Atene e delle Missioni Italiane in Oriente, Volume 95, 2017 95, 143.

[28] Hackel, T., Wegner, J.D., Schindler, K., 2016. Contour detection in unstructured 3d point clouds, in: Proceedings of the IEEE conference on computer vision and pattern recognition, pp. 1610–1618.

[29] Hallager, E., Papadopoulou, E., Tzachili, I., 2012. VRY S (4/4) 01– The first hieroglyphic inscription from western Crete. Kadmos 50, 63–74. doi:10.1515/KADMOS.2011.004.

[30] HeliconSoft, a. Helicon focus. Helicon Focus. URL: https://www.heliconsoft.com/heliconsoft-products/helicon-focus/. accessed: 2020-09-24.

[31] HeliconSoft, b. Helicon remote. Helicon Remote. URL: https://www.heliconsoft.com/heliconsoft-products/helicon-remote/. accessed: 2020-09-24.

[32] HeliconSoft, . Helicon remote: setting focus bracketing parameters. https://www.heliconsoft.com/HeliconRemoteHelp/english/HeliconRemote.html}HR_FOCUS_BRACKETING. URL: https://www.heliconsoft.com/HeliconRemoteHelp/english/HeliconRemote.html}HR_FOCUS_BRACKETING. data retrieved: 2021-09-20.

[33] HeliconSoft, 2015. Helicon filter help - stacking. https://www.heliconsoft.com/filter/help/english/stacking.html. Online; ac-

cessed March, 2021.

[34] HeliconSoft, 2018. Understanding the Focus Stacking Parameters. https://www.heliconsoft.com/helicon-focus-main-parameters/. Online; accessed November, 2018.

[35] Hermon, S., Polig, M., Driessen, J., Jans, G., Bretschneider, J., 2018. An integrated 3D shape analysis and scientific visualization approach to the study of a Late Bronze Age unique stone object from Pyla-Kokkinokremos, Cyprus. Digital Applications in Archaeology and Cultural Heritage 10, e00075. doi:10.1016/j.daach.2018.e00075.

[36] INSCRIBE, 2018. INSCRIBE project website. https://site.unibo.it/inscribe/en/about-1.

[37] INSCRIBE, 2020. 3D Interactive Web Viewer. www.inscribercproject.com/3d_viewer_home.php.

[38] Jacobsen, K., 2013. Characteristics and accuracy of large area covering height models. The International Archives of the Photogrammetry, Remote Sensing and Spatial Information Sciences 1, 157–162. doi:10.5194/isprsarchives-XL-1-W1-157-2013.

[39] Kontogianni, G., Chliverou, R., Koutsoudis, A., Pavlidis, G., Georgopoulos, A., 2017. Enhancing close-up image based 3d digitisation with focus stacking. The International Archives of the Photogrammetry, Remote Sensing and Spatial Information Sciences 42. doi:10.5194/isprs-archives-XLII-2-W5-421-2017.

[40] Kumar, S., Snyder, D., Duncan, D., Cohen, J., Cooper, J., 2003. Digital preservation of ancient cuneiform tablets using 3D-scanning, in: Fourth International Conference on 3-D Digital Imaging and Modeling, 2003. 3DIM 2003. Proceedings., IEEE. pp. 326–333. doi:10.1109/IM.2003.1240266.

[41] Lastilla, L., Ravanelli, R., Ferrara, S., 2019a. 3D high-quality modeling of small and complex archaeological inscribed objects: Relevant issues and proposed methodology. The International Archives of the Photogrammetry, Remote Sensing and Spatial Information Sciences XLII-2/W11, 699–706. doi:10.5194/isprs-archives-XLII-2-W11-699-2019.

[42] Lastilla, L., Ravanelli, R., Valério, M., Ferrara, S., 2019b. 3D modelling of the Mamari tablet from the Rongorongo corpus: Acquisition, processing issues, and outcomes. The International Archives of the Photogrammetry, Remote Sensing and Spatial Information Sciences XLII-2/W18, 85–89. doi:10.5194/isprs-archives-XLII-2-W18-85-2019.

[43] Lastilla, L., Ravanelli, R., Valério, M., Ferrara, S., 2021. Modelling the Rongorongo tablets: A new transcription of the Échancrée tablet and the foundation for decipherment attempts. Digital Scholarship in the Humanities URL: https://academic.oup.com/dsh/advance-article/doi/10.1093/llc/fqab045/6387816?guestAccessKey=c7841dea-2e5e-4e48-b978-01c0e27272d6, doi:10.1093/llc/fqab045.

[44] Luhmann, T., Robson, S., Kyle, S., Boehm, J., 2019. Close-Range Photogrammetry and 3D Imaging. De Gruyter. URL: https://doi.org/10.1515/9783110607253, doi:doi:10.1515/9783110607253.

[45] Lussu, P., Marini, E., 2020. Ultra close-range digital photogrammetry in skeletal anthropology: A systematic review. PloS one 15, e0230948. doi:10.1371/journal.pone.0230948.

[46] McCamy, C.S., Marcus, H., Davidson, J.G., 1976. A color-rendition chart. Journal of Applied Photographic Engineering 2, 95–99.

[47] Micheletti, N., Chandler, J., Lane, S.N., 2005. Structure from motion (SFM) photogrammetry, in: Geomorphological Techniques. British Society for Geomorphology. chapter 2, pp. 1–12. URL: http://www.geomorphology.org.uk/sites/default/files/geom_tech_chapters/2.2.2_sfm.pdf.

[48] Molada-Tebar, A., Marqués-Mateu, A., Lerma, J.L., 2019. Correct use of color for cultural heritage documentation. The International Annals of the Photogrammetry, Remote Sensing and Spatial Information Sciences IV-2/W6, 107–113. doi:10.5194/isprs-annals-IV-2-W6-107-2019.

[49] Mudge, M., Malzbender, T., Schroer, C., Lum, M., 2006. New reflection transformation imaging methods for rock art and multiple-viewpoint display, in: Ioannides, M.; Arnold, D.; Niccolucci, F. & Mania, K., eds., The 7th International Symposium on Virtual Reality, Archaeology and Cultural Heritage, Vast. pp. 195–202. doi:10.2312/VAST/VAST06/195-202.

[50] Olivier, J.P., Godart, L., 1996. Corpus hieroglyphicarum inscriptionum Cretae: Études crétoises. École Française d'Athènes.

[51] Percoco, G., Guerra, M.G., Salmeron, A.J.S., Galantucci, L.M., 2017. Experimental investigation on camera calibration for 3d photogrammetric scanning of micro-features for micrometric resolution. The International Journal of Advanced Manufacturing Technology 91, 2935–2947.

[52] Porter, S.T., Roussel, M., Soressi, M., 2016. A Simple Photogrammetry Rig for the Reliable Creation of 3D Artifact Models in the Field: Lithic Examples from the Early Upper Paleolithic Sequence of Les Cottés (France). Advances in Archaeological Practice 4, 71–86. doi:10.7183/2326-3768.4.1.71.

[53] Potenziani, M., Callieri, M., Dellepiane, M., Corsini, M., Ponchio, F., Scopigno, R., 2015. 3DHOP: 3D Heritage Online Presenter. Computers & Graphics 52, 129–141. URL: https://www.sciencedirect.com/science/article/pii/S0097849315001041, doi:https://doi.org/10.1016/j.cag.2015.07.001.

[54] Potenziani, M., Callieri, M., Scopigno, R., 2018. Developing and maintaining a web 3D viewer for the CH community: an evaluation of the 3DHOP framework., in: 16th Eurographics Workshop on Graphics and Cultural Heritage (2018). doi:10.2312/gch.20181356.

[55] Prager, C.M., Gronemeyer, S., Wagner, E., 2020. Shedding New Light on the Maya Stela from Hix Witz in Stuttgart. Technical Report. Bonn: Nordrhein-Westfälische Akademie der Wissenschaften und der Künste. doi:10.20376/IDIOM-23665556.20.rn016.en.

[56] Ravanelli, R., Lastilla, L., Nascetti, A., Di Rita, M., Nigro, L., Montanari, D., Spagnoli, F., Crespi, M., 2018. 3D modelling of archaeological small finds by the structure sensor range camera: comparison of different scanning applications. Applied Geomatics 10, 399–413. doi:10.1007/s12518-018-0215-5.

[57] Remondino, F., Guarnieri, A., Vettore, A., 2005. 3D modeling of close-range objects: photogrammetry or laser scanning?, in: Videometrics VIII, International Society for Optics and Photonics. p. 56650M. doi:10.1117/12.586294.

[58] Rothacker, L., Fisseler, D., Müller, G.G., Weichert, F., Fink, G.A., 2015. Retrieving cuneiform structures in a segmentation-free word spotting framework, in: Proceedings of the 3rd International Workshop on Historical Document Imaging and Processing, pp. 129–136.

[59] Sapirstein, P., 2018. A high-precision photogrammetric recording system for small artifacts. Journal of Cultural Heritage 31, 33–45. doi:10.1016/j.culher.2017.10.011.

[60] Snavely, N., Seitz, S.M., Szeliski, R., 2008. Modeling the world from internet photo collections. International journal of computer vision 80, 189–210.

[61] V-GER, 2021. ScanRider 1.2. https://www.vger.eu/brand/v-ger/scanrider-1-2. URL: https://www.vger.eu/brand/v-ger/scanrider-1-2. accessed: 2021-10-14.

[62] Valente, R., Barazzetti, L., 2020. Methods for ancient wall graffiti documentation: Overview and applications. Journal of Archaeological Science: Reports 34, 102616. doi:10.1016/j.jasrep.2020.102616.

[63] Vergne, R., Pacanowski, R., Barla, P., Granier, X., Schlick, C., 2010. Radiance scaling for versatile surface enhancement, in: Proceedings of the 2010 ACM SIGGRAPH symposium on Interactive 3D Graphics and Games, pp. 143–150. doi:10.1145/1730804.1730827.

[64] Wessel, B., Huber, M., Wohlfart, C., Marschalk, U., Kosmann, D., Roth, A., 2018. Accuracy assessment of the global tandem-x digital elevation model with gps data. ISPRS Journal of Photogrammetry and Remote Sensing 139, 171–182. doi:10.1016/j.isprsjprs.2018.02.017.

[65] Westoby, M., Brasington, J., Glasser, N., Hambrey, M., Reynolds, J., 2012. Structure-from-Motion photogrammetry: A low-cost, effective tool for geoscience applications. Geomorphology 179, 300–314. URL: https://www.sciencedirect.com/science/article/pii/S0169555X12004217, doi:https://doi.org/10.1016/j.geomorph.2012.08.021.

[66] X-Rite, 2020. Colorchecker camera calibration. ColorChecker Camera Calibration v 2.0 X-Rite. URL: https://xritephoto.com/ph_product_overview.aspx?ID=938ŹAction=SupportŹSoftwareID=2030.

accessed: 2020-09-24.